Monthly Notices of the ROYAL ASTRONOMICAL SOCIETY

MNRAS **493,** 5807–5815 (2020)
Advance Access publication 2020 March 13

doi:10.1093/mnras/staa683

Supersolar metallicity in G0–G3 main-sequence stars with $V < 15$. II. An extension of the sample

M. Chávez,[1⋆] C. Tapia-Schiavon,[1,2] E. Bertone[1] and R. López-Valdivia[3]

[1] Instituto Nacional de Astrofísica, Óptica y Electrónica, Luis Enrique Erro 1, Tonantzintla, Puebla 72840, Mexico
[2] Instituto de Radioastronomía y Astrofísica, Universidad Nacional Autónoma de Mexico, Apdo. Postal 3-72 (Xangari), 58090 Morelia, Michoacán, México
[3] Department of Astronomy, The University of Texas at Austin, 2515 Speedway, Stop C1400, Austin, TX 78712-1205, USA

Accepted 2020 February 28. Received 2020 February 24; in original form 2019 November 4

ABSTRACT

We present the spectroscopic analysis at intermediate resolution of a new sample of 146 Sun-like stars (of spectral types G0–G3 and luminosity class V), which complements the data set of 233 targets previously investigated. Aimed at identifying objects with supersolar metallicity, we conducted observations at the Observatorio Astrofísico Guillermo Haro and derived the basic stellar atmospheric parameters, namely the effective temperature, surface gravity, and global metallicity, based on a set of absorption spectroscopic indices in the wavelength region 3800–4800 Å. The newly derived set of parameters is in good agreement with previous determinations collected from sources in the literature. Considering the full sample of our investigation (379 stars), we also compared the effective temperatures of stars in common (354 objects) with *Gaia* DR2 for which temperatures are available, and found that, on average, our values are about 100 K higher. We show that most of the largest temperature discrepancies can plausibly be ascribed to interstellar extinction effects on *Gaia*'s photometry. Finally, within the working sample we found four more stars that present supermetallicity, one of which was previously reported in the literature.

Key words: Stars: atmospheres – stars: fundamental parameters – stars: solar-type.

1 INTRODUCTION

More than 50 yr ago, Spinrad & Taylor (1969) presented the pioneer work on stellar supermetallicity, that is, stars with a global chemical abundance, in excess of that found in the Sun, beyond a given threshold. That paper considered the then accepted metallicity of the Hyades ([Fe/H] = +0.2 dex) as the limit to identify supermetal-rich (SMR) stars and served as the basis of a number of studies in both extragalactic and Milky Way scenarios. While SMR stars have probably not been studied as profusely as their very metal poor counterparts, as the latter represent a fossil record of the early chemical contents and evolution of Universe, they have furnished fundamental insights on evolutionary aspects of more evolved extragalactic populations. For instance, it is now well established that ellipticals, preferentially the massive ones (e.g. Buzzoni 1995; Thomas, Maraston & Schawinski 2010; Saracco et al. 2019), display the supermetallicity phenomenon, as well as bulges of spirals, including those of the Milky Way (see the early work of Rich 1988) and M31 (Saglia et al. 2018). In addition, the SMR populations have motivated the construction of spectroscopic data bases aimed at extending the observational and theoretical ingredients required in the synthesis of stellar populations to model and study the integrated spectra of unresolved metal-rich stellar assemblies (e.g. Buzzoni et al. 2001).

In the solar neighbourhood, chemical composition in general and SMR stars in particular have been a subject of numerous investigations as they furnish important clues on the star formation history and chemical evolutionary properties of the Galaxy. In fact, recent studies have been devoted to study the chemical, kinematic, and dynamical properties of SMR stars with the aim of explaining the mere presence and origin of stars with supersolar metal content in the vicinity of the Sun, which can be plausibly interpreted as the result of radial migration, if stars are old enough, from the inner spheroidal component (e.g. Chen et al. 2019, and references therein).

Studies of supermetallicity in stars have regained momentum in the past two decades. The interest has been boosted by the correlation found between stellar chemical composition and the presence of giant exoplanets: The prevalence of massive planets in short orbits significantly increases if the host star presents high metal abundances (e.g. Gonzalez 1998; Santos, Israelian & Mayor 2001; Fischer & Valenti 2005). Through the analysis of thousands of exoplanetary systems with homogeneously derived stellar parameters (see Sousa et al. 2018), it has been possible to investigate the origin of such a relationship, known as the

⋆ E-mail: mchavez@inaoep.mx

giant planet–metallicity correlation, as well as to test different planet formation scenarios. To date, analyses favour the primordial origin for the high metallicity of the giant exoplanet host stars, and planet formation appears to be better explained by the core accretion scenario (Alibert, Mordasini & Benz 2004) than as the product of disc instabilities (Boss 1997). The reader is referred to the recent and extensive review of Adibekyan (2019) for more details.

In Lopez-Valdivia et al. (2014), hereafter Paper I, we presented the analysis of a first sample of 233 stars, limited in magnitude ($V < 15$ mag), with spectral types between G0 and G3 and luminosity class V. The study was based on spectroscopic observations at intermediate resolution [full width at half-maximum (FWHM) 2.5 Å] collected at the Observatorio Astrofísico Guillermo Haro (OAGH). We defined a set of 41 Lick-like indices in the spectral range of 3800–4800 Å and found a fiducial set of 10 indices that allowed the determination of the leading photospheric parameters, namely effective temperature ($T_{\rm eff}$), surface gravity ($\log g$), and global metallicity ([M/H]). That study yielded 213 targets for which the stellar parameters were derived for the first time and incremented by 10 per cent (20 new objects) the number of reported SMR ([Fe/H] $\geq +0.16$ dex) stars listed in the 2010 version of the PASTEL catalogue of stellar parameters (Soubiran et al. 2010).

The above metallicity value also follows a Hyades-based chemical composition limit and represents a conservative threshold of more recent metallicity estimates of the cluster by Heiter et al. (2014), [Fe/H] $= +0.13 \pm 0.06$ dex, and of those provided by Netopil et al. (2016), which are based on three different procedures, of [Fe/H] $= +0.13 \pm 0.05$, $+0.14 \pm 0.04$, and $+0.15 \pm 0.03$ dex, derived from high- and low-quality spectroscopic data and from photometry, respectively.

In this second paper of the series, we present the analysis of an additional sample of 146 Sun-like stars with the same limiting visual magnitude. As in Paper I, the aim is to derive the leading atmospheric parameters and to identify SMR targets, by maintaining [M/H] $\geq +0.16$ dex[1] as the limit, that can be either used as templates in stellar population synthesis techniques and as objectives for giant planet searches.

2 THE STELLAR SAMPLE, OBSERVATIONS AND DATA REDUCTION

For the sake of easy reference, in this section we briefly describe the assembly of the stellar sample, the collection of spectroscopic data and reductions, processes already reported in detail in Paper I. The original working sample, selected back in 2008 from the SIMBAD[2] data base, is composed of about 1200 stellar objects that were compliant of four selection criteria, namely objects must have spectral types between G0 and G3, a luminosity class concordant with main-sequence (MS) stars, a visual magnitude $V < 15$, and a declination of $\delta > -10°$. In this paper, we complement the 233 stars reported in Paper I with 146 more targets observed during 2014–2016 at the same premises and, with the exception of the CCD camera, also the same instrumental set-up as our initial sample. This is, observations were conducted at the OAGH (in the northern state of Sonora, Mexico) with the 2.12-m telescope and the Boller and Chivens spectrograph, equipped with an SITe 1024 × 1024 CCD. The grating of 600 l mm^{-1} and the slit width of 200 μm provided a constant spectral resolution of 2.5 Å FWHM and a dispersion of 0.84 Å pixel^{-1} along the wavelength range between 3800 and 4800 Å. As for the data set in Paper I, we acquired at least two spectroscopic images for each star, with total exposure times between 3 min, for the brighter objects, and about 60 min for the fainter ones, to reach a typical signal-to-noise ratio per pixel of about 40–90, computed in a window of 100 Å around 4600 Å.

Table 1. The sample of the observed solar analogues. The full table is available in the electronic version.

Name	V (mag)	Spectral type
HD 100796	8.41	G0V
HD 102161	8.39	G3V
HD 104076	8.40	G0V
HD 107087	8.04	G0V
HD 110276	9.07	G0Vw
HD 110523	9.33	G1V
HD 110950	8.18	G2V
HD 113785	8.67	G0V
HD 115762	8.52	G2V
HD 117845	8.09	G2V
HD 120566	9.00	G2V
HD 121149	8.55	G0V
HD 128611	9.00	G6V
HD 129135	8.38	F7V (G0V)

The sample is presented in Table 1, where we list the star identification, the V magnitude, and the spectral type given in SIMBAD as of 2019 May. In the extended sample studied in this paper, there are 19 objects (like HD 129135 in Table 1) that do not accomplish the required selection criteria. They now either ascribed a hotter or colder classification, or do not include a luminosity class. We have searched in the literature and found that, indeed, for 18 stars there exists a source for the previously assigned spectral type and luminosity class and most probably the modification corresponds to an SIMBAD upgrade in the past 11 yr with more recent spectroscopic studies. The only exception is the star BD+11 2369 for which we were not able to find a luminosity class, but it has been labelled as a possible subdwarf (class IV) by Lee (1984) and considered as an MS by Nissen & Schuster (2012). We have left these targets in the rest of the analysis and added (in parenthesis) in Table 1 the previous spectral classification. A brief discussion on some of those targets is given in Section 4.

In Fig. 1, we show the V magnitude distribution of the extended sample presented in this paper (solid line) and the 233 stars reported in Paper I (dash–dotted line). Most stars in both samples are located in the interval $8 \leq V \leq 11$ mag; however, the Paper I sample includes more objects fainter than $V = 10$ mag, which corresponds to an initial decision of focusing the observing runs on less studied targets that lacked determinations of their stellar parameters.

In order to obtain a solar reference with the same instrumental set-up, we again observed the solar spectrum reflected by the asteroids Vesta and Ceres, and also included that of Metis. As we shall see later, these observations allowed us to confirm that the method we have implemented to derive stellar parameters (and uncertainties)

[1]Throughout this paper, we denote with [M/H] the global chemical composition in the theoretical spectra and derived parameters from them. [Fe/H] is used for the iron content derived through the analysis of individual species of observed spectra. These two notations are equivalent if a target follows solar-scaled abundances, as is the case of the theoretical data base implemented in this work. They can be different if abundances of individual species, other that iron, appear enhanced or depleted.
[2]http://simbad.u-strasbg.fr/simbad/

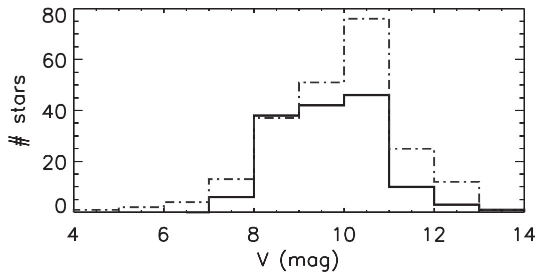

Figure 1. Distribution of *V* magnitude for the targets included in this paper (solid line) and in Paper I (dash–dotted line).

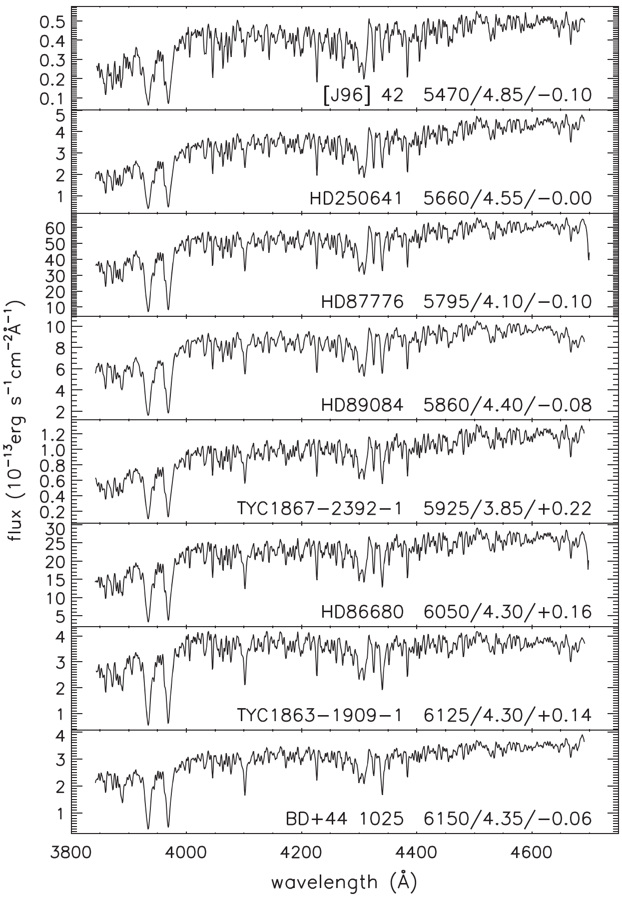

Figure 2. Spectra of an illustrative subset of stars in the extended sample. In each panel, along with the star's name, the atmospheric parameters (in the format T_{eff}/log *g*/[M/H]) are indicated.

is robust and provides reliable parameters, in particular T_{eff} and [M/H].

We applied the standard reduction scheme within IRAF: bias subtraction, flat-field correction, cosmic ray removal, wavelength calibration (using an internal HeAr lamp), and flux calibration (using spectrophotometric standard stars from the ESO list[3]). The wavelength calibration was double checked and corrected for radial velocity. Fig. 2 depicts the spectra of eight representative objects, indicating in each case the set of derived parameters, obtained as explained in Section 3.

[3]http://www.eso.org/sci/observing/tools/standards/spectra/stanlis.html

3 STELLAR PARAMETERS DERIVED FROM ABSORPTION LINE SPECTROSCOPIC INDICES

Aimed at determining T_{eff}, log *g*, and [M/H] of the targets through the use of spectroscopic indices, we have implemented the same process described in detail in Paper I, which essentially consists of the following two steps:

(i) Calculate the fiducial set of 10 spectroscopic indices, defined by Worthey & Ottaviani (1997), Trager et al. (1998), Carretero (2007), and Lee et al. (2008), that quantify the flux absorption of the most relevant features within the considered wavelength interval (see table 3 of Paper I). This is done in both the empirical data set, described in the previous section, and in theoretical spectra computed at the same resolution. The latter aspect was already done in Paper I, based on the grid of Munari et al. (2005), but with finer steps in the parameter space. We remind the reader that the process included a re-calibration of the theoretical indices to account for the potential discrepancies between theory and observations, mainly attributable to opacity calculations. It is also important to remark that the 10 indices were selected from a much larger set (41 indices) based on the capabilities of separating the effects of different atmospheric parameters.

(ii) Conduct a comparison between observed and theoretical indices that provide the best fit. This fit is obtained through a least squares method that minimizes the statistic:

$$\chi^2 = \frac{1}{n}\sum_{i=1}^{n}\frac{\left(I_{\mathrm{i,teo}} - I_{\mathrm{i,obs}}\right)^2}{\sigma^2_{\mathrm{i,obs}}}, \tag{1}$$

where $I_{\mathrm{i,\,teo}}$ and $I_{\mathrm{i,\,obs}}$ are the theoretical index and the observational index, respectively, n is the total number of indices, and $\sigma_{\mathrm{i,\,obs}}$ is the error associated with each index of the observed spectrum. The combination of theoretical stellar parameters, whose indices provide the minimum χ^2, was assigned to the corresponding star. It is important to remark that the estimate of $\sigma^2_{\mathrm{i,obs}}$ was critical for the minimization of χ^2 and somewhat challenging in view of the difficulty of deriving the noise directly from the spectra, characterized by numerous atomic and molecular transitions. Because of its importance and for the sake of easier reference, below we summarize the procedure we have followed in Paper I, also adopted in this work, to derive $\sigma^2_{\mathrm{i,obs}}$.

The error used in equation (1) was calculated through an iterative process that consisted in three steps. In the first step, we assumed that the noise in an observed stellar spectrum is represented by the average of a moving standard deviation over the maximum wavelength interval included in the index band definition, i.e. from the bluer edge of the blue band to the redder limit of the red band. In a second step, we considered that the noise is the standard deviation of a Gaussian distribution and is randomly added to each wavelength point in the index bands of the observed spectrum. This process is repeated 1000 times, for each of which we calculated the index value. The standard deviation of this collection of values is incorporated in equation (1) to derive a set of stellar parameters. In the third step, we interpolated, within the theoretical spectral library, the set of parameters to obtain the corresponding synthetic spectrum that is subtracted to the observed one in order to compute the residual flux, where the contribution of the line absorption to the flux variation is decreased. This residual spectrum was adopted in the first step and the process was repeated until two consecutive iterations resulted in the same atmospheric parameters. The reader is referred to Paper I for more details.

Table 2. Solar atmospheric parameters from the asteroids observations.

Object	T_{eff} (K)	$\sigma_{T_{eff}}$ (K) +	$\sigma_{T_{eff}}$ (K) −	log g (dex)	$\sigma_{\log g}$ (dex) +	$\sigma_{\log g}$ (dex) −	[M/H] (dex)	$\sigma_{[M/H]}$ (dex) +	$\sigma_{[M/H]}$ (dex) −
VESTA	5775	45	50	4.65	0.20	0.20	−0.06	0.04	0.04
CERES	5765	45	45	4.60	0.20	0.20	−0.06	0.04	0.04
METIS	5755	45	45	4.60	0.20	0.20	−0.06	0.04	0.04

Table 3. Stellar atmospheric parameters. (The full version of the table is available in an electronic form as Supporting Information in the online version of the article.)

Object	T_{eff} (K)	$\sigma_{T_{eff}}$ (K) +	$\sigma_{T_{eff}}$ (K) −	log g (dex)	$\sigma_{\log g}$ (dex) +	$\sigma_{\log g}$ (dex) −	[M/H] (dex)	$\sigma_{[M/H]}$ (dex) +	$\sigma_{[M/H]}$ (dex) −
HD 100796	5960	65	40	3.85	0.40	0.20	0.00	0.04	0.04
HD 102161	5775	55	55	3.85	0.35	0.25	− 0.02	0.04	0.06
HD 104076	5870	30	40	4.20	0.20	0.20	− 0.02	0.02	0.04
HD 107087	6025	75	80	3.90	0.40	0.40	0.00	0.08	0.08
HD 110276	6145	20	25	4.95	0.00	0.10	− 0.18	0.04	0.02
HD 110523	5880	45	65	4.20	0.25	0.35	0.14	0.04	0.06
HD 110950	5930	95	120	3.80	0.55	0.60	− 0.02	0.10	0.14
HD 113785	6215	40	40	4.55	0.20	0.20	− 0.06	0.02	0.02
HD 115762	5470	120	175	3.70	0.55	0.65	− 0.16	0.18	0.24
HD 117845	5930	115	125	4.05	0.60	0.65	− 0.24	0.10	0.12
HD 120566	6030	20	35	4.90	0.05	0.15	− 0.34	0.02	0.04
HD 121149	5895	70	30	3.75	0.35	0.20	0.02	0.10	0.04

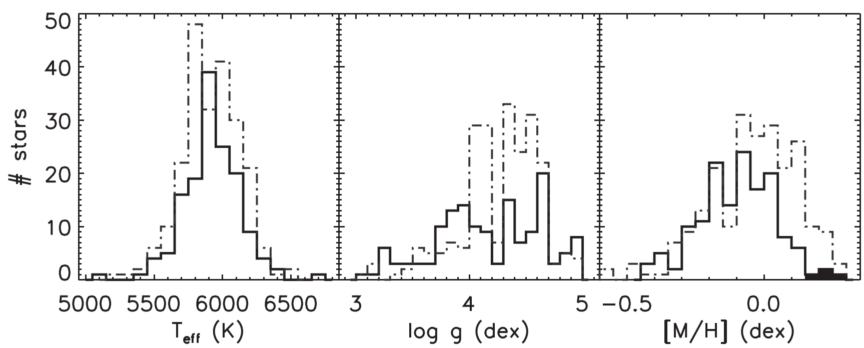

Figure 3. Atmospheric parameter distributions of the extended sample (solid line) and, for comparison, those of Paper I (dot–dashed line). The black area shows the four newly identified SMR stars.

In Table 2, we list the set of atmospheric parameters for the Sun, and the corresponding uncertainties, derived from the spectra of the three asteroids. While T_{eff} and log g are compatible with the accepted solar values ($T_{eff,\odot} = 5772$ K, log $g_\odot = 4.44$ dex) to within 1σ, the metallicity deviation is slightly larger but equal for all three objects ([M/H] = −0.06 dex), as are the uncertainties. Therefore, we added a value of 0.06 dex to the [M/H] scale, for the stellar sample, in order to transform it to the solar reference.

In Table 3, we list the derived set of atmospheric parameters and the corresponding uncertainties of the stellar sample. The distributions of the resulting atmospheric parameters are displayed in Fig. 3. The solid line histograms correspond to the extended sample, while dot–dashed histograms indicate the distribution of stars of Paper I. For T_{eff} both distributions are highly compatible, with maxima at about T_{eff} = 5900 K, and in overall agreement with the spectral types used as selection criteria. For the log g, we discussed in Paper I that our implementation of spectroscopic indices to derive this parameter yields a large dispersion of the determined values, nevertheless, as can be noticed in the mid-panel of Fig. 3, most of the values have log g > 3.7 dex for the sample of this work and log g > 4.0 dex for the targets analysed in Paper I. The presence of low-gravity objects probably indicates that the sample includes many stars that already left the MS and are evolving through the subgiant phase. The gravities of such objects are expected to be of the order of 3.9 dex, according to the values compiled by E. Mamajek.[4]

Finally, for the overall metallicity of the new sample, our values peak close to solar chemical composition, at [M/H] = −0.1 dex, with the distribution skewed towards subsolar metallicity. Note that the sample in Paper I contains more stars with [M/H] > −0.1 dex distributed around the solar metallicity. The black bins indicate the four metal-rich stars identified in this work (see Section 5).

Several objects clearly deviate from the depicted distributions and for which we consider that the spectral classification should be revised. For instance, inherent to T_{eff}, the star BD+34 2417 is classified as a G0V star in SIMBAD and the original source is Tchipashvili (1973). However, in the absence of interstellar

[4]http://www.pas.rochester.edu/ emamajek/IV_standards_PASTEL_logg.txt

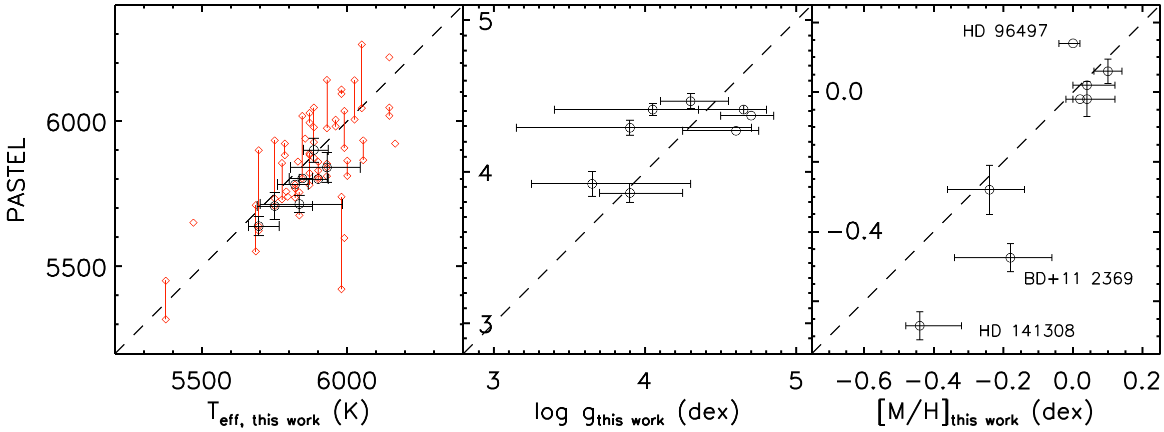

Figure 4. Comparison of the atmospheric parameters determined in this work and the values included in the PASTEL catalogue. The dashed line indicates the slope unity. The black circles indicate the eight stars with sources in the literature that provide simultaneously the three parameters, while the red diamonds in the left-hand panel display the values from works that only determined the $T_{\rm eff}$; when a star has more than one value, the points are connected.

extinction (Ruiz-Dern et al. 2018), the $T_{\rm eff}$ of 5075 K we have derived and the $B - V$ colour of 0.98 (Høg et al. 2000) place it as a K2–K3-type star. On the high temperature side, the star BD+15 2538 was ascribed as a G0V class (Nassau & Macrae 1955). We determined a $T_{\rm eff}$ of 6715 K, which would correspond to an F3V object according to Pecaut & Mamajek (2013). Moreover, its $B - V = 0.23$ (Høg et al. 2000) implies an even earlier spectral class (A8V).

4 COMPARISON WITH PREVIOUS WORKS

As in Paper I, we conducted a comparison of the derived parameters with other data sets. Such a comparison serves to identify potential systematic trends and eventually attempts to diminish the discrepancies. For this comparison, we opted to compare our data with the most updated version of the PASTEL catalogue (Soubiran et al. 2016) that includes many sources in the literature: 33 sources in our data set are included in PASTEL and the parameter comparisons are displayed in Fig. 4. In the left-hand panel, we illustrate the comparison for $T_{\rm eff}$ (red diamonds), in which, whenever a target has two or more determinations of $T_{\rm eff}$, the points are connected. The black circles in all the panels correspond to the eight stars for which the three atmospheric parameters are available from the same literature source.[5] For these stars, atmospheric parameters, including chemical abundances, are derived from high-resolution spectroscopic observations. The overall behaviour indicates that our $T_{\rm eff}$ values are slightly overestimated, on average: 59 K if we only consider this latter sample of eight objects, or 19 K if we take into account all temperature differences (the red points in the left-hand panel of Fig. 4). The most deviant object is HD 68744, a G0V star, for which we determine $T_{\rm eff} = 5980$ K, while the two references in PASTEL provide 5422 (Masana, Jordi & Ribas 2006) and 5740 K (Casagrande et al. 2011). The uncertainties reported by those authors and ours cannot account for the observed discrepancies, in particular the nearly 600 K with respect to the $T_{\rm eff}$ of Masana et al. (2006). The star has $B - V = 0.60$ mag, a value that, in the absence of reddening, is perfectly compatible with a G0 star on the MS (Pecaut & Mamajek 2013); therefore, a plausible option is that the *K*-band photometry, used in Masana et al. (2006), is affected by some systematic effects or that the *K*-band flux is polluted by circumstellar material. For this particular object, note that the difference between the literature values is also large (318 K), in spite of being derived from similar methods. In order to understand this inconsistency, a comparison of all stars in common in both works is suggested.

The central panel of Fig. 4 indicates that log g values are in agreement, even though their dispersion is substantial, due to the large errors that we determined. For the case of [M/H] (right-hand panel of Fig. 4), we compare our values with the [Fe/H] given in PASTEL. Three objects, BD+11 2369, HD 141308, and HD 96497, labelled in the figure, show the largest discrepancies. Our results for these stars indicate a global metal contents of −0.18, −0.44, and +0.00 dex, respectively, and the differences with the reported values in PASTEL are $[M/H]_{\rm ours} - [Fe/H]_{\rm PASTEL} = +0.30, +0.23$, and −0.14 dex. For the stars BD+11 2369 and HD 141308, both with $[Fe/H] < -0.4$ dex in PASTEL, our [M/H] values can be explained considering that the objects are strongly α-enhanced: BD+11 2369 has Mg, Si, Ca, and Ti enhanced, with respect to Fe, by about 0.3 dex, according to Nissen & Schuster (2010), while HD 141308 has $[O/Fe] = +0.46$ dex and an enhancement larger than 0.2 dex for Mg, Al, Si, Ca, Ti, as reported by Bensby et al. (2014). Therefore, for the same value of Fe, the metal mass fraction is higher than that in the solar-scaled models that we used, producing a higher [M/H]. In the case of HD 96497, the [Fe/H] value comes from Takeda et al. (2007), but no error is reported in that work.

Recently, results from the *Gaia* mission (Gaia Collaboration 2018) have been released, together with accompanying papers that describe the details on the followed procedures for deriving atmospheric parameters, including the $T_{\rm eff}$ of more than 160 million stars brighter than $G = 17$ mag (Andrae et al. 2018). The *Gaia* data set allows the comparison with the vast majority of our determinations, including those in Paper I, as the validity range of *Gaia*'s $T_{\rm eff}$ estimates (3000–10 000 K) fully inscribes the range of our derived values. The $T_{\rm eff}$ comparison of the 354 common targets

[5]The eight stars and the literature sources of the parameters reported in PASTEL are BD+11 2369 (Nissen & Schuster 2010; Nissen et al. 2014), HD 91950, HD 117845 (Ramírez, Allende Prieto & Lambert 2013), HD 141308 (Bensby, Feltzing & Oey 2014), HD 41708 (Ramírez et al. 2013; Datson, Flynn & Portinari 2015), HD 71227, HD 87680, and HD 96497 (Takeda et al. 2007). In the case of BD+11 2369 and HD 41708, we computed the average of two measurements. Errors are not reported in PASTEL for all stars.

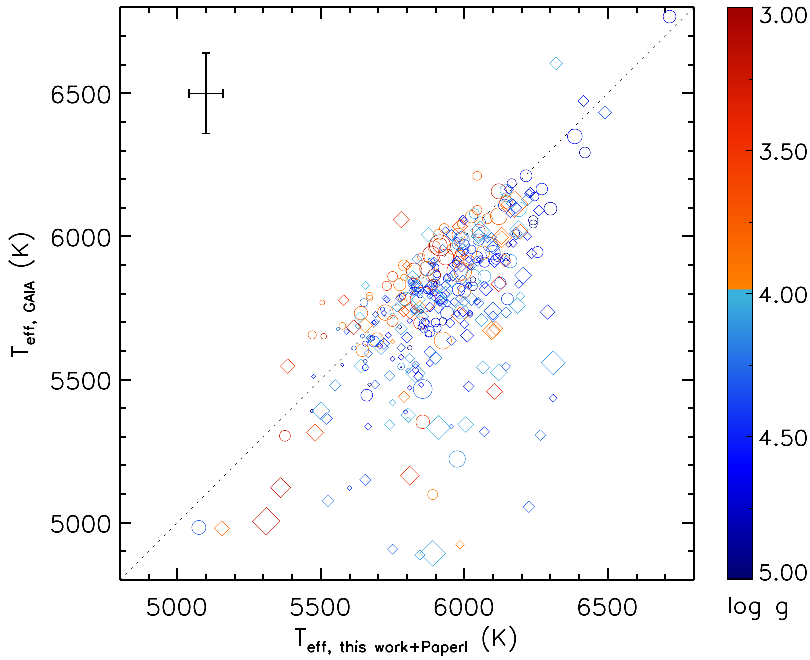

Figure 5. Comparison of our determined $T_{\rm eff}$ and those reported by the *Gaia* team (Andrae et al. 2018). The diamond symbols represent data from Paper I and the circles for stars in the extension of the sample. The average uncertainties are shown in the upper left corner. Symbol sizes are proportional to the luminosity of the stellar sample, provided by *Gaia*. The symbol colour indicates the log g from this work and Paper I, according to the scale of the colour bar on the right.

with a fiducial Priam flag (Andrae et al. 2018; see its appendix B) is depicted in Fig. 5. In this plot, the diamond symbols stand for objects of Paper I and the circles for stars of the extended sample presented in this article. The sizes of the symbols are proportional to the luminosity, which ranges from $L = 0.40\,{\rm L}_{\odot}$ to $55\,{\rm L}_{\odot}$, of the sources as also provided by *Gaia* (Andrae et al. 2018). The colour scale indicates our determination of log g, spanning the interval from 3.0 to 5.0 dex, as defined in the colour bar. For the sake of clarity, error bars are not included, but the typical uncertainty is indicated in the upper left of the panel.

Most stars are clustered in a relatively narrow temperature interval (5600–6200 K) and slightly below the slope unity indicated with a dotted line. There are, nevertheless, numerous targets that display a pronounced discrepancy, one in excess of 1000 K. It is difficult to furnish an explanation based solely on the quite different methodology followed by the two data sets. Note, however, that the vast majority of the most deviant stars are in the fainter side of the sample, having $V > 10$ mag (only 2 of 35 stars with an absolute $T_{\rm eff}$ difference larger than 400 K are brighter). Considering that our method is based on spectroscopic indices that are barely dependent on the shape of the spectral continuum, one plausible interpretation is that the interstellar extinction affects the broad-band *Gaia* colours, at least of some of the stars.

In order to verify such an assumption, we have plotted in Fig. 6 the $\Delta T_{\rm eff} = T_{\rm eff,\,thiswork\,+\,Paper\,I} - T_{\rm eff,\,Gaia}$ versus the *Gaia* distance (Bailer-Jones et al. 2018). One can notice that the largest disparities ($\Delta T_{\rm eff} > 300$ K) are seen for objects more distant than 125 pc, inscribed in the upper right rectangle. The filled circles in this plot depict those objects that are excluded after an iterative σ-clipping performed over the distribution of the differences. The clipping threshold has been assumed as the value, in a Gaussian distribution of the temperature difference, such that the probability that $\Delta T_{\rm eff}$ is greater than this value is $1/N$, where N is the number of objects of the retained sample at each iteration. This procedure provided

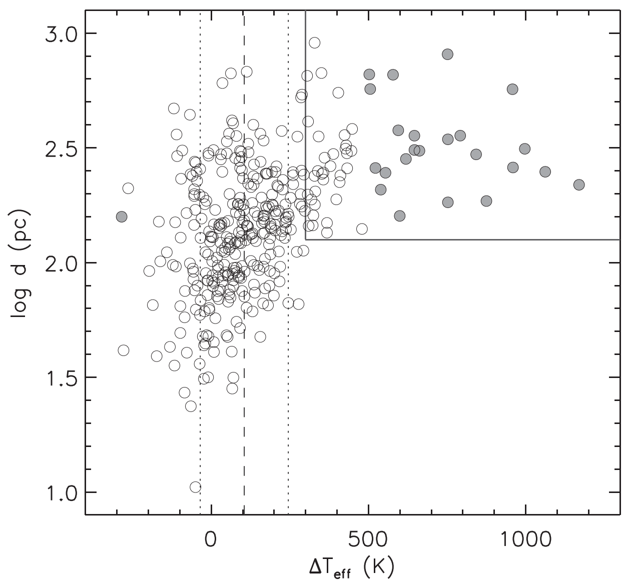

Figure 6. $\Delta T_{\rm eff}$ versus distance of the stars of the samples in this work and Paper I. The filled grey circles depict the most deviant targets that were removed after a σ-clipping process. The vertical dashed and dotted lines indicate the average $\Delta T_{\rm eff}$ plus and minus one standard deviation. The upper right rectangle circumscribes the stars with $\Delta T_{\rm eff} > 300$ K and at a distance larger than 125 pc.

thresholds of about 2.75σ, which translates to a $\Delta T_{\rm eff}$ decreasing from 589 to 384 K, from the first to the last iteration. Once we removed the outliers, the resulting distribution is very symmetrical with a mean difference of $\Delta T_{\rm eff} = 105$ K and $\sigma = 140$ K, values that quantitatively contrast the two temperature scales. The objects within the rectangle appear either at low galactic latitudes ($|b| < 10^{\circ}$)

Table 4. Comparison summary: average difference and standard deviation.

	$\overline{\Delta}_{\rm our-other}$	σ
PASTEL		
$T_{\rm eff}$ (K) 8 stars	+59	43
$T_{\rm eff}$ (K) 66 data	+18	139
log g (dex)	−0.03	0.31
[M/H] (dex)	+0.07	0.13
Gaia		
$T_{\rm eff}$ (K)	+105	140

or in regions close to the galactic anticentre, where the interstellar medium shows patchy extensions down to $b \sim -34^{\circ}$ at galactic longitudes of about 160° (e.g. Schlafly & Finkbeiner 2011).

The above comparison points towards that some *Gaia* targets require a revision of the $T_{\rm eff}$. Such a revision has been anticipated by Andrae et al. (2018), in addition to the derivation of surface gravity and metallicity, an extension that will valuably help to avoid parameter degeneracies (Buzzoni et al. 2001; Bertone et al. 2004).

In Table 4, we summarize the results of the comparison presented in the previous lines. In column 1, we indicate the data set from which the figures have been calculated, namely the eight stars with the three parameters derived from spectroscopic data, the stars in common with the PASTEL catalogue and the *Gaia* sample. In the second and third columns, we list, respectively, the average difference between our values and those in PASTEL and *Gaia*, and the standard deviation of the residuals.

4.1 Some comments on SIMBAD reclassified stars and low-gravity objects

For some targets that appear reclassified in SIMBAD, our $T_{\rm eff}$ values look in agreement with the updated spectral class. For instance, the star HD 155105, previously classified as a G3V (Moore & Paddock 1950) and now as a G8V, has a derived temperature compatible with G8–G9 ($T_{\rm eff}$ = 5375 K). Similarly, BD+45 2018 has a $T_{\rm eff}$ of 5575 K, more consistent with the updated G5 class than for the previously assigned G2. Conversely, other two stars are now also classified as G5 (and lack of a luminosity class), namely BD+43 2143 and BD+44 2244, but our results indicate temperatures expected for G1–G2 stars (5905 and 5860 K, respectively). Inherent to log g, we note that, to within our uncertainties, 17 out of the 19 newly classified stars in SIMBAD have high log g and the remaining two (HD 131428 and HD 155105) present values more appropriate to subgiant objects. In fact, the *Gaia* luminosities (Andrae et al. 2018) of these two objects are, respectively, 8.2 $L_{\odot}$ and 2.4 $L_{\odot}$, when the expected values, if on the MS, should be about 1.4 $L_{\odot}$ and 0.6 $L_{\odot}$.[6] In some other instances, in spite of the ascribed luminosity class V, we derived rather low gravities, which appear to be confirmed by the high luminosities reported in the *Gaia* data set. Some of the most extreme cases have luminosities in excess of 10 $L_{\odot}$: for example, HD 131024, HD 77051, and HD 84219; the latter having $L = 34.29\, L_{\odot}$. As indicated in Paper I, it is beyond the scope of the paper series to reclassify stars, but the above analysis motivates us to revise the classification of several stars, as well as conduct more detailed spectroscopic analyses at high resolution.

[6]From the Eric Mamajek compilation at http://www.pas.rochester.edu/ emamajek/EEM_dwarf_UBVIJHK_colors_Teff.txt.

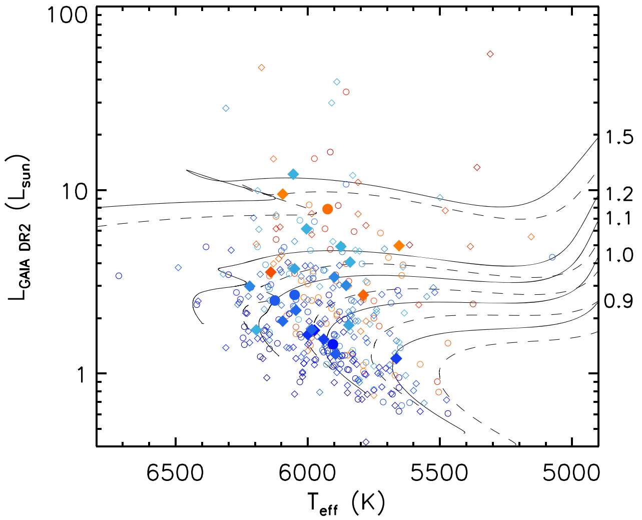

Figure 7. HR diagram of the samples in this work and Paper I. The diamond symbols represent data from Paper I and the circles for stars of this work. The SMR stars are shown with larger filled symbols. Colours stand as in Fig. 5. Evolutionary tracks, for the masses (in $M_{\odot}$) indicated beyond the right side of the panel and for [M/H] = −0.02 (solid curves) and +0.14 dex (dashed curves), are also displayed.

5 THE SMR STARS

The main goal of this paper is to complement the set of previously identified stars (22 objects) that display supermetallicity ([M/H] $\geq$ +0.16). After the above analysis, we added four more objects: BD+43 2143, HD 86680, TYC 1863-1909-1, and TYC 1867-2392-1. Of these, only HD 86680 has previous chemical composition determination from spectroscopy (e.g. Gaspar, Rieke & Ballering 2016; Deka-Szymankiewicz et al. 2018) and from *ubvy*-H β photometry (Karatas, Bilir & Schuster 2005), all works attribute supersolar metallicity to this object. For the other three targets, the values derived in this paper represent the first determination of [M/H]. We want to point out that, for TYC 1867-2392-1, we might be dealing with an evolved object. While, to within uncertainties, our gravity value (log $g = 3.85^{+0.20}_{-0.25}$ dex) is consistent with an MS object, the luminosity derived from *Gaia* (7.8 $L_{\odot}$) indicates that it has already attained a luminosity five times larger than that expected for an object on the MS, assuming the $T_{\rm eff}$ we have derived.

In Fig. 7, we show the Hertzsprung–Russell (HR) diagram constructed considering the luminosities from *Gaia* and our set of $T_{\rm eff}$. For a comparison, we have also included a set of evolutionary tracks (Bressan et al. 2012), for masses appropriate for MS G-type stars, with metallicity near solar ([M/H] = −0.02 dex) and near our SMR limit (+0.14 dex). We also added 1.5 $M_{\odot}$ tracks, appropriate for an MS early-F star. It is interesting to note that, while the majority of objects are located close to the MS, numerous stars appear in more advance evolutionary stages, more prominently the star HD 290084, whose luminosity reaches 55 $L_{\odot}$. Almost half of the SMR objects are in fact located in the subgiant branch region. These are also the SMR stars for which we derive low values of log g. In particular, the three SMR stars with the largest luminosities are located not far from the 1.5 $M_{\odot}$ track along the subgiant branch.

Finally, a simple but illustrative exercise aimed at elucidating the origin of the SMR stars in our sample is to derive the kinematic properties of the objects and establish their membership to the different galactic components (thick or thin discs). For the 26 SMR

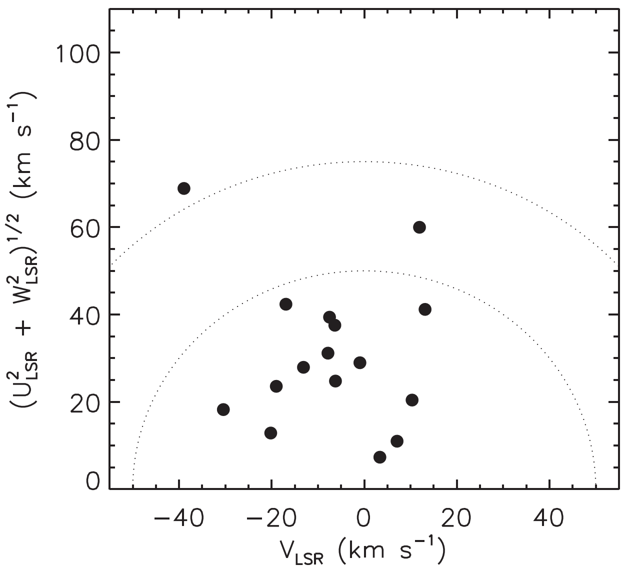

Figure 8. Toomre diagram for 16 SMR stars. The dotted curves indicates v_{tot} constant values of 50 and 75 km s^{-1}.

stars, we have searched within the *Gaia* DR2 for the necessary parameters (the parallax, the projected proper motion in right ascension and declination, and the radial velocity V_r) to calculate the space-velocity components of the targets: 14 of our targets have data. For other two stars, BD+47 3218 and HD 228356, V_r was obtained from the works of Sandage & Fouts (1987) and Costado et al. (2017), respectively. For the particular case of HD 228356, we used the median value reported in Costado et al. (2017).

The above input parameters were used to get the Galactic space-velocity components, relative to the local standard of rest (LSR; Coşkunoğlu et al. 2011): U_{LSR}, V_{LSR}, and W_{LSR} and the total velocity $v_{tot} = (U^2_{LSR} + V^2_{LSR} + W^2_{LSR})^{1/2}$. The parameters' uncertainties are mostly within 3 per cent of the reported value, except for V_r for which, in many instances, the errors are larger than 1 km s^{-1}. With the calculated Galactic velocities, we constructed the Toomre diagram depicted in Fig. 8. Stars with $v_{tot} < 50$ km s^{-1} are most probably thin-disc stars, while thick-disc objects are expected to be located beyond a 75 km s^{-1} boundary (see e.g. Bensby et al. 2005; Fig. 1). The object that has the largest v_{tot} is BD+60 600 (79 km s^{-1}), the most metal-rich star, therefore the only probable thick-disc star in our sample.

6 SUMMARY AND CONCLUSIONS

A set of the leading atmospheric parameters (T_{eff}, log g, and [M/H]) was determined for a sample of 146 stars, which complement the 233 objects presented in Paper I. The goal of this investigation was to identify a fiducial set of SMR stars that could be targeted, for instance, in giant planet searches. In addition to the 22 stars identified in Paper I, we report four more objects, one of which might not be on the MS, as indicated by its luminosity.

We compared our derived parameters with other sources in the literature and, to within uncertainties, our values match well, as was the case of the targets in Paper I. However, in the process, we identified several stars that most probably need to be reclassified and, for some others that lack of a luminosity class in the updated information in SIMBAD, we confirm that they are objects on the MS, based on the high log g values.

The availability of the *Gaia* DR2 allowed the T_{eff} comparison for the majority of the targets in our full sample. Such an analysis delivered an interesting by-product in which we establish that the overall difference in the temperature scales between both data sets is about 100 K, with our determinations being higher, and that there are still stars, in the *Gaia*'s clean sample, that could presumably be affected by interstellar extinction. This result goes in line with the *Gaia*'s group incentive of carrying out independent analyses that could lead to the identification of limitations and quality of the parameters provided by the *Gaia* team (see section 7.6 in Gaia Collaboration 2018).

ACKNOWLEDGEMENTS

The authors want to thank the anonymous referee. Her/his comments were very useful to improve the presentation of the paper. They also thank the mexican Consejo Nacional de Ciencia y Tecnologia (CONACYT) for financial support through grant CB-2015-256961. This research has made use of the SIMBAD data base, operated at CDS, Strasbourg, France.

REFERENCES

Adibekyan V., 2019, Geosciences, 9, 105
Alibert Y., Mordasini C., Benz W., 2004, A&A, 417, L25
Andrae R. et al., 2018, A&A, 616, 8
Bailer-Jones C. A. L., Rybizki J., Fouesneau M., Mantelet G., Andrae R., 2018, AJ, 156, 5
Bensby T., Bensby T., Feltzing S., Lundström I., Ilyin I., 2005, A&A, 433, 185
Bensby T., Feltzing S., Oey M. S., 2014, A&A, 562, 71
Bertone E., Buzzoni A., Chávez M., Rodríguez-Merino L. H., 2004, AJ, 128, 829
Boss A. P., 1997, Science, 276, 1836
Bressan A., Marigo P., Girardi L., Salasnich B., Dal Cero C., Rubele S., Nanni A., 2012, MNRAS, 427, 127
Buzzoni A., 1995, ApJS, 98, 69
Buzzoni A., Chavez M., Malagnini M. L., Morossi C., 2001, PASP, 113, 1365
Carretero C., 2007, PhD thesis, Instituto de Astrofísica de Canarias (IAC)
Casagrande L., Schönrich R., Asplund M., Cassisi S., Ramírez I., Meléndez J., Bensby T., Feltzing S., 2011, A&A, 530, 138
Chen Y. Q., Zhao G., Zhao J. K., Liang X. L., Wu Y. Q., Jia Y. P., Tian H., Liu J. M., 2019, AJ, 158, 249
Costado M. T., Alfaro E. J., González M., Sampedro L., 2017, MNRAS, 465, 3879
Coşkunoğlu B. et al., 2011, MNRAS, 412, 1237
Datson J., Flynn C., Portinari L., 2015, A&A, 574, 124
Deka-Szymankiewicz B., Niedzielski A., Adamczyk M., Adamów M., Nowak G., Wolszczan A., 2018, A&A, 615, 31
Fischer D. A., Valenti J., 2005, ApJ, 622, 1102
Gaia Collaboration, 2018, A&A, 616, 1
Gaspar A., Rieke G. H., Ballering N., 2016, ApJ, 826, 171
Gonzalez G., 1998, A&A, 334, 221
Heiter U., Soubiran C., Netopil M., Paunzen E., 2014, A&A, 561, 93
Høg E. et al., 2000, A&A, 355, 27
Karatas Y., Bilir S., Schuster W. J., 2005, MNRAS, 360, 1345
Lee S. G., 1984, AJ, 89, 702
Lee Y. S. et al., 2008, AJ, 136, 2022
López-Valdivia R., Bertone E., Chávez M., Tapia-Schiavon C., Hernández-Águila J. B., Valdés J. R., Chavushyan V., 2014, MNRAS, 444, 2251
Masana E., Jordi C., Ribas I., 2006, A&A, 450, 735
Moore J. H., Paddock G. F., 1950, ApJ, 112, 48
Munari U., Sordo R., Castelli F., Zwitter T., 2005, A&A, 442, 1127
Nassau J. J., Macrae D. A., 1955, ApJ, 121, 32

Netopil M., Paunzen E., Heiter U., Soubiran C., 2016, A&A, 585, 150
Nissen P. E., Schuster W. J., 2010, A&A, 511, L10
Nissen P. E., Schuster W. J., 2012, A&A, 543, 28
Nissen P. E., Chen Y. Q., Carigi L., Schuster W. J., Zhao G., 2014, A&A, 568, 25
Pecaut M. J., Mamajek E. E., 2013, ApJS, 208, 9
Ramírez I., Allende Prieto C., Lambert D. L., 2013, ApJ, 764, 78
Rich R. M., 1988, AJ, 95, 828
Ruiz-Dern L., Babusiaux C., Arenou F., Turon C., Lallement R., 2018, A&A, 609, 116
Saglia R. P., Opitsch M., Fabricius M. H., Bender R., Blaña M., Gerhard O., 2018, A&A, 618, 156
Sandage A., Fouts G., 1987, AJ, 93, 592
Santos N. C., Israelian G., Mayor M., 2001, A&A, 373, 1019
Saracco P., La Barbera F., Gargiulo A., Mannucci F., Marchesini D., Nonino M., Ciliegi P., 2019, MNRAS, 484, 2281
Schlafly E. F., Finkbeiner D. P., 2011, ApJ, 737, 103
Soubiran C., Le Campion J. F., Cayrel de Strobel G., Caillo A., 2010, A&A, 515, 111
Soubiran C., Le Campion J. F., Broullet N., Chemin L., 2016, A&A, 591, 118
Sousa S. G. et al., 2018, A&A, 620, 58
Spinrad H., Taylor B. J., 1969, ApJ, 157, 1279
Takeda Y., Kawanomoto S., Honda S., Ando H., Sakurai T., 2007, A&A, 468, 663
Tchipashvili D. G., 1973, Abastumanskaya Astrofiz. Obs. Byull., 44, 3
Thomas D., Maraston C., Schawinski K., 2010, MNRAS, 404, 1775
Trager S. C., Worthey G., Faber S. M., Burstein D., Gonzalez J. J., 1998, ApJS, 116, 1
Worthey G., Ottaviani D. L., 1997, ApJS, 111, 377

SUPPORTING INFORMATION

Supplementary data are available at *MNRAS* online.

Table 1. The sample of the observed solar analogues.
Table 3. Stellar atmospheric parameters.

Please note: Oxford University Press is not responsible for the content or functionality of any supporting materials supplied by the authors. Any queries (other than missing material) should be directed to the corresponding author for the article.

This paper has been typeset from a TEX/LATEX file prepared by the author.